



Cite this: *Dalton Trans.*, 2019, **48**, 9776

Received 5th March 2019,
Accepted 1st April 2019

DOI: 10.1039/c9dt00971j
rsc.li/dalton

A d^{10} Ag(I) amine–borane σ -complex and comparison with a d^8 Rh(I) analogue: structures on the η^1 to $\eta^2:\eta^2$ continuum†

Alice Johnson, ^a Antonio J. Martínez-Martínez, ^a Stuart A. Macgregor ^{*b} and Andrew S. Weller ^{*a}

$H_3B\cdot NMe_3$ σ -complexes of d^8 $[(L1)Rh][BAr^F_4]$ and d^{10} $[(L1)Ag][BAr^F_4]$ (where **L1** = 2,6-bis-[1-(2,6-diisopropylphenylimino)ethyl]pyridine) have been prepared and structurally characterised. Analysis of the molecular and electronic structures reveal important but subtle differences in the nature of the bonding in these σ -complexes, which differ only by the identity of the metal centre and the d-electron count. With Rh the amine–borane binds in an $\eta^2:\eta^2$ fashion, whereas at Ag the unsymmetrical $\{Ag\cdots H_3B\cdot NMe_3\}$ unit suggests a structure lying between the $\eta^2:\eta^2$ and η^1 extremes.

Introduction

Transition metal σ -complexes, in which an E–H bond (e.g., E = H, B, C, Si) binds with a metal centre through a 3-centre 2-electron interaction, are of fundamental interest due to their central role in E–H activation.¹ For example, amine–borane σ -complexes,² exemplified by $[M]\cdots H_3B\cdot NRH_2$ (Fig. 1), are key intermediates in the catalytic dehydropolymerisation of amine–boranes that leads to the formation of B–N polymeric materials,^{3–5} B–B coupling⁶ or hydroboration reactions.⁷

$H_3B\cdot NMe_3$ is often used as a model substrate for such processes as it provides insight into the initial binding step of the amine–borane, there being no protic N–H available for onward reaction. Transition metal σ -complexes of $H_3B\cdot NMe_3$ have been reported across the transition metal series,⁵ e.g. for group 6 (**A**),² 7,⁸ 8 (ref. 9) and 9 (**B**, **C**).^{6,10} Both η^1 and $\eta^2:\eta^2$ binding modes of $H_3B\cdot NMe_3$ have been observed, depending on the steric and electronic demands of the metal, Fig. 1(ii), and the principal bonding interaction can be described by σ -donation from the B–H bond into an empty metal d orbital.² Recently the isolation of the first $H_3B\cdot NMe_3$ σ -complex of a group 11 metal was reported, the d^{10} Cu(I) complex **D**, with a $\eta^2:\eta^2$ -bound $H_3B\cdot NMe_3$. Analysis of the bonding showed that the bent $\{CuL_2\}$ fragment presents a LUMO largely of 4s character that receives

electron density from the B–H bonds, while back bonding was negligible.^{11,12} This is a relatively rare example a coinage metal^{13–17} that shows close interactions with E–H bonds.

We report here a straightforward route to a $H_3B\cdot NMe_3$ σ -complex of the coinage metal Ag(I), complex **1** Fig. 1(iii), that is supported by the pincer ligand 2,6-bis-[1-(2,6-diisopropylphenylimino)ethyl]pyridine, **L1**. Such highly tuneable ligands have been used, for example, with Fe and Co centres in olefin polymerisation catalysis.^{18,19} They also support the generation

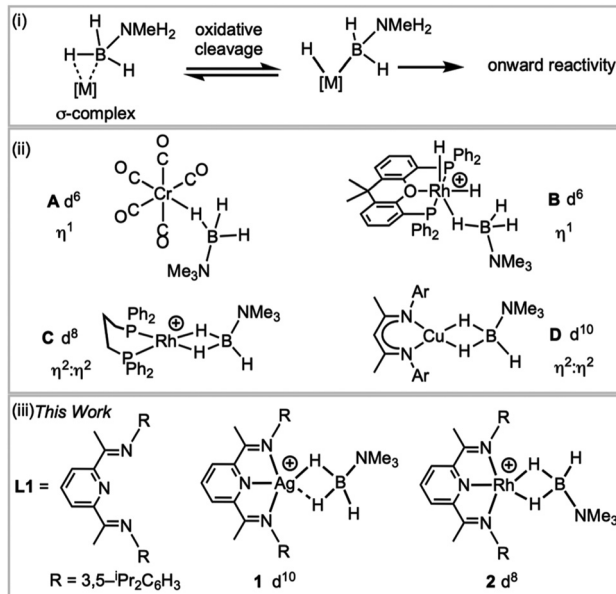


Fig. 1 (i) H–B activation; (ii) examples of σ -amine–borane complexes, (iii) complexes reported in this work. $[BAr^F_4]^-$ anions are not shown.

^aChemistry Research Laboratories, Department of Chemistry, University of Oxford, Oxford, OX1 3TA, UK. E-mail: andrew.weller@chem.ox.ac.uk

^bInstitute of Chemical Sciences, Heriot Watt University, Edinburgh EH14 4AS, UK. E-mail: S.A.Macgregor@hw.ac.uk

† Electronic supplementary information (ESI) available: Synthesis, characterisation data, structures of **3**, **7** and **8**, computational details. CCDC 1895514–1895519. For ESI and crystallographic data in CIF or other electronic format see DOI: 10.1039/c9dt00971j



of latent low coordinate Ag(i) complexes, *e.g.* $(\text{L})\text{AgOTf}$ ($\text{OTf} =$ triflate), that coordinate arenes;^{20,21} while $(\text{L})\text{RhCl}$ have been used as precursors for nanoparticle dehalogenation catalysts²² ($\text{L} = 2,6\text{-bis-[1-(2,6-}R\text{-phenylimino)ethyl]pyridine}$). The synthesis of a directly analogous σ -complex of Rh(i), 2, is also reported here. This offers a rare opportunity to directly compare the structures, bonding and NMR spectroscopic reporters for mono-cationic d^8 and d^{10} σ -complexes in systems where only the identity of the metal is changed.

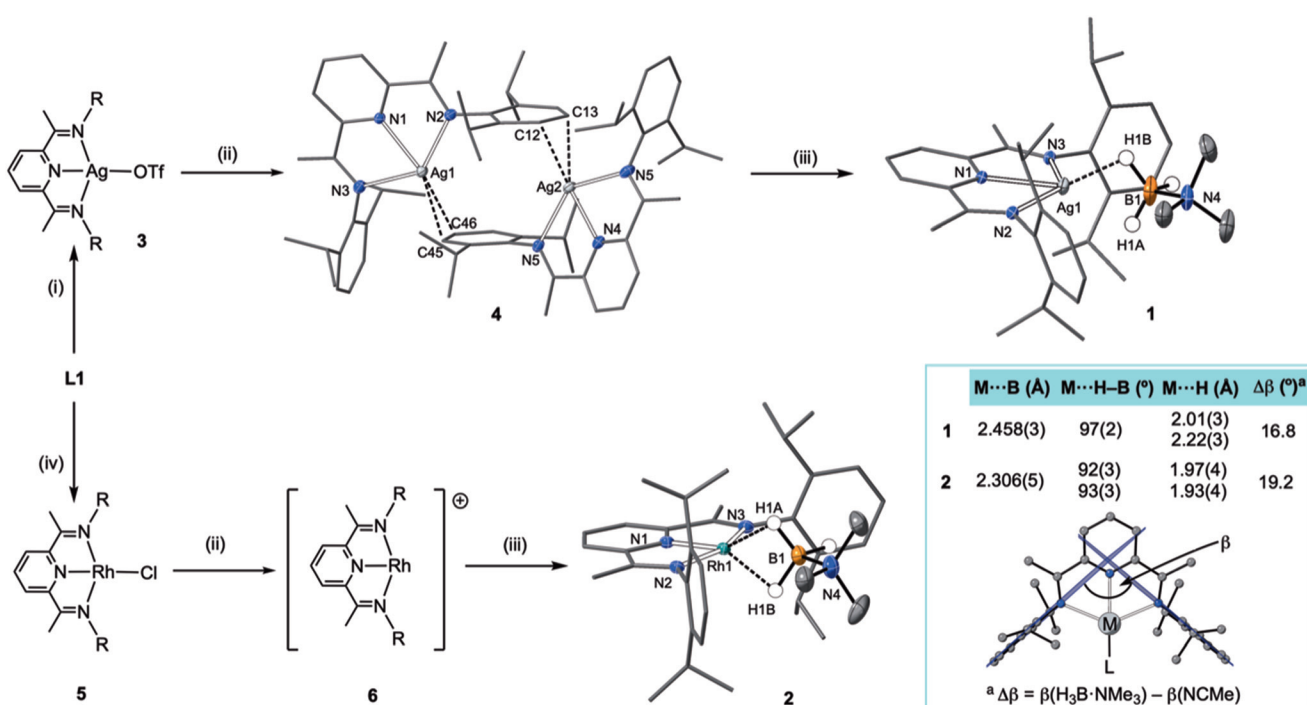
Results and discussion

An appropriate operationally unsaturated precursor for the synthesis of a $\text{H}_3\text{B}\cdot\text{NMe}_3$ adduct of Ag(i) is the arene-bridged dimeric complex $[(\text{L1})\text{Ag}]_2[\text{BAr}^{\text{F}}_4]_2$, 4 (Scheme 1), which comes from addition of $\text{Na}[\text{BAr}^{\text{F}}_4]$ to $(\text{L1})\text{AgOTf}$, 3, itself prepared by addition of $\text{Ag}[\text{OTf}]$ to free L1. The synthesis and structure of monomeric complex 3 is detailed in the ESI.[†]

In the solid-state complex 4 is a solvent-free, weakly associated dimer, which approaches coordinative saturation through η^2 interactions with the aryl groups on a neighbouring ligand. There is no crystallographically imposed symmetry. The $\text{Ag}\cdots\text{C}$ 2.439(6)–2.623(6) Å. They are comparable, but generally longer, than distances found in a Ag(i)–N-heterocyclic carbene

arene-bridged dimer [2.444(4), 2.348(4) Å],²³ or $[(\text{L})\text{Ag}(\eta^2\text{-toluene})][\text{OTf}]$ [2.464(7) Å].²⁰ The appearance of a very simple ^1H NMR spectrum for 4 as signalled by a single ^1Pr -environment even at 183 K (CD_2Cl_2), suggests these weak silver–arene interactions are not retained in solution, or at the very least the molecule is highly fluxional, as the solid-state structure (even allowing for time-averaged C_2 symmetry) would be expected to show 4 different ^1Pr groups. DOSY (Diffusion-Ordered Spectroscopy) experiments determined the diffusion coefficients for complexes 3 and 4 in CD_2Cl_2 to be very similar ($1.166 \pm 0.014 \times 10^{-9} \text{ m}^2 \text{ s}^{-1}$ for 3 and $1.126 \pm 0.013 \times 10^{-9} \text{ m}^2 \text{ s}^{-1}$ for 4), suggesting 4 is a monomer in solution, likely a CD_2Cl_2 adduct similar to that observed for a Ag(i)–N-heterocyclic carbene complex reported by Rivard and co-workers.²³ Consistent with this latent coordinative unsaturation, addition of one equivalent (per Ag) of $\text{H}_3\text{B}\cdot\text{NMe}_3$ to 4 gave the air- and light-stable, bright yellow σ -complex $[(\text{L1})\text{Ag}(\text{H}_3\text{B}\cdot\text{NMe}_3)][\text{BAr}^{\text{F}}_4]$, 1, isolated in 98% yield. Similarly, addition of one equivalent of $\text{Na}[\text{BAr}^{\text{F}}_4]$ ²⁴ to $(\text{L1})\text{RhCl}$ 5²⁵ in CH_2Cl_2 affords the known latent-coordinatively unsaturated 6,²⁶ which also likely exists as an adduct in CH_2Cl_2 solution,²⁷ that forms a σ -complex $[(\text{L1})\text{Rh}(\text{H}_3\text{B}\cdot\text{NMe}_3)][\text{BAr}^{\text{F}}_4]$ 2 with $\text{H}_3\text{B}\cdot\text{NMe}_3$, which can be isolated as a dark green solid (79% yield).

The molecular structures of 1 and 2 were determined by single crystal X-ray diffraction (Scheme 1). For both, the high quality of the data allowed for the BH_3 hydrogens to be located



Scheme 1 Synthesis of complexes 1–6. (i) $\text{Ag}[\text{OTf}]$, CH_2Cl_2 ; (ii) $\text{Na}[\text{BAr}^{\text{F}}_4]$, CH_2Cl_2 ; (iii) $\text{H}_3\text{B}\cdot\text{NMe}_3$, CH_2Cl_2 ; (iv) $\frac{1}{2}[\text{Rh}(\text{C}_2\text{H}_4)_2\text{Cl}]_2$, toluene. $\text{R} = 3,5\text{-}^1\text{Pr}_2\text{C}_6\text{H}_3$. Selected bond lengths [\AA] and angles [$^{\circ}$]: 1: $\text{Ag1}\cdots\text{H1A}$, 2.22(3); $\text{Ag1}\cdots\text{H1B}$, 2.01(3); $\text{Ag1}\cdots\text{N1}$, 2.3737(13); $\text{Ag1}\cdots\text{N2}$, 2.4306(13); $\text{Ag1}\cdots\text{N3}$, 2.4303(13); $\text{Ag1}\cdots\text{B1}$, 2.458(3); $\text{N4}\cdots\text{B1}$, 1.609(3); $\text{N1}\cdots\text{Ag1}\cdots\text{B1}$, 171.33(8); $\text{N3}\cdots\text{Ag1}\cdots\text{N2}$, 134.14(5). 2: $\text{Rh1}\cdots\text{H1A}$, 1.97(4); $\text{Rh1}\cdots\text{H1B}$, 1.93(4); $\text{Rh1}\cdots\text{N1}$, 1.910(2); $\text{Rh1}\cdots\text{N2}$, 2.061(2); $\text{Rh1}\cdots\text{N3}$, 2.050(2); $\text{Rh1}\cdots\text{B1}$, 2.306(5); $\text{N1}\cdots\text{B1}$, 1.588(8); $\text{N}\cdots\text{Rh1}\cdots\text{B1}$, 169.12(15); $\text{N2}\cdots\text{Rh1}\cdots\text{N3}$, 156.76(9); ellipsoids at the 30% probability level. 4: $\text{Ag1}\cdots\text{C45}$, 2.525(7); $\text{Ag1}\cdots\text{C46}$, 2.571(7); $\text{Ag2}\cdots\text{C12}$, 2.439(6); $\text{Ag2}\cdots\text{C13}$, 2.623(6) Å. Hydrogen atoms, other than those at boron, and $[\text{BAr}^{\text{F}}_4]^-$, are omitted for clarity. Inset shows key structural metrics for the σ -interactions.



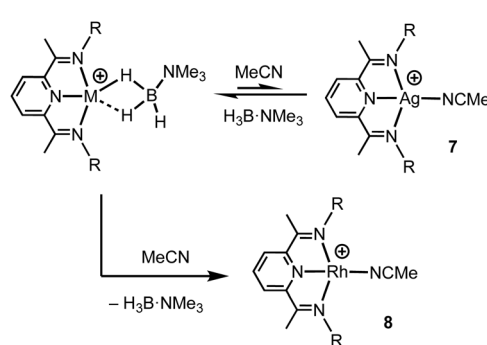
and freely refined. The different electron configurations of the d^8 Rh(i) and d^{10} Ag(i) centres lead to subtle differences in the coordination geometry about each metal centre. In both cases a κ^3 -binding of **L1** is observed, albeit with considerably longer Ag–N distances [2.3737(13)–2.4306(13) Å] than Rh–N [1.910(2)–2.061(2) Å], even taking into account the small difference in covalent radii (Rh, 1.42; Ag, 1.45 Å). This may simply reflect a weaker binding of Ag compared to Rh.

Turning to the interaction of the borane with the metal centre, in complex **1** the Ag–B distance [2.458(3) Å] is comparable to other Ag–H–B interactions, *e.g.* Ag(PPh₃)(CB₁₁H₁₂) [2.504(3) Å].²⁸ One B–H is closer to Ag (H1B), but the other (H1A) is not much further removed [2.01(2) and 2.22(3) Å respectively], while the M–H(1B)–B angle is rather open [97(2)°]. The bonding in **1** therefore appears to approach $\eta^2:\eta^2$, *i.e.* the limiting structure found for **D**, as η^1 coordination of the B–H bond would be expected to give a much wider angle and longer M–B distance.¹³ For complex **2** the H₃B–NMe₃ ligand clearly adopts a more symmetrical $\eta^2:\eta^2$ binding mode, with a corresponding shorter Rh–B distance [2.306(5) Å], equivalent M–H–B angles, and M–H distances that are the same. While the Rh–B distance is long compared to other amine–borane σ -complexes of Rh(i) that show $\eta^2:\eta^2$ binding, *e.g.* **C** [2.199(3) Å], it is shorter than found for η^1 binding, *e.g.* **B** [2.759(6) Å].⁶ This lengthening may be due to the steric effects with flanking {³Pr₂C₆H₃} groups. To measure such effects, in a self-consistent manner, we have prepared and structurally characterised (ESI†) the corresponding MeCN adducts (Scheme 2), $[(\mathbf{L1})\text{Ag}(\text{NCMe})][\text{BAr}^{\text{F}}_4]$, **7**, and $[(\mathbf{L1})\text{Rh}(\text{NCMe})][\text{BAr}^{\text{F}}_4]$, **8**, by addition of 100 equivalents or one equivalent of MeCN respectively to the corresponding amine–borane complexes.²⁹ The linear nitrile offers a minimal steric profile and thus baselines the metal–ligand geometry, and in particular the angle formed between the two planes that the aryl rings define (β), Scheme 1 inset. Coordination of the amine–borane results in the aryl groups moving apart, and this is measured as $\Delta\beta$ between the two structures. That this is slightly larger for complex **2** compared with **1** [19.2° *versus* 16.8°] confirms the greater steric pressure in the more strongly bound Rh-complex. Interestingly, the local coordination environment around Rh, with the σ -amine–borane {H₂B} motif

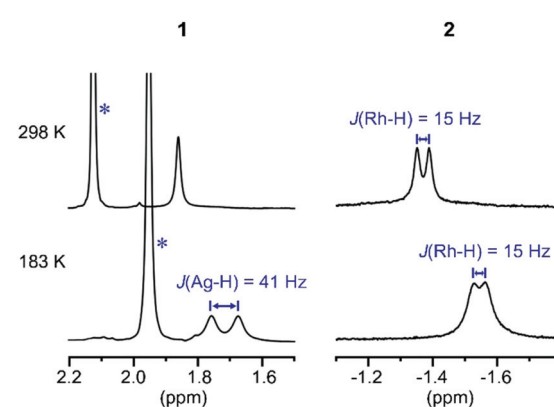
sitting orthogonal to the ligand plane is reminiscent of the bonding mode calculated for the closely related, but much less stable, σ -methane complex $[\text{Rh}(\text{PONOP})(\text{H}_2\text{CH}_2)][\text{BAr}^{\text{F}}_4]$ [$\text{PONOP} = \kappa^3\text{-2,6-(}^4\text{Bu}_2\text{PO)}_2\text{C}_5\text{H}_3\text{N}$],³⁰ although in this case an η^2 -structure is slightly favoured over the symmetric $\eta^2:\eta^2$ motif.

These subtle structural differences are carried over into the solution NMR data. For **1** the BH₃ group is observed as a singlet at δ 1.82 in the 298 K $^1\text{H}\{^{11}\text{B}\}$ NMR spectrum (CD₂Cl₂), shifted slightly downfield compared to the free ligand [δ 1.64] (Scheme 3). At 183 K this separates into a broad doublet due to coupling to $^{107/109}\text{Ag}$ [$J(\text{AgH}) = 41$ Hz], confirmed by measurement at two different spectrometer frequencies, alongside a temperature-induced chemical shift. This signal did not resolve into terminal and coordinated B–H resonances, suggesting a low energy exchange, even at 183 K. The loss of coupling at higher temperature suggests an exchange process that involves rapid and reversible H₃B–NMe₃ decoordination. In the ^{11}B NMR spectrum the amine–borane is observed as a broad quartet at δ –16.3, shifted upfield compared to free H₃B–NMe₃ in CD₂Cl₂ [δ –8.3, $\Delta\delta$ –8]. The NMR data for complex **2** are subtly different. The BH₃ group is observed as a doublet at δ –1.37 [$J(\text{RhH}) = 15.1$ Hz] in the 298 K $^1\text{H}\{^{11}\text{B}\}$ NMR spectrum. This coupling constant does not change upon lowering the temperature to 183 K, indicative of both fast exchange and a process that retains the borane bound with the metal centre. We propose a hemilabile $\eta^2:\eta^2-\eta^1-\eta^2:\eta^2$ fluxional process, as has been calculated³¹ in related systems. The ^{11}B NMR signal for complex **2** shows a broad singlet at δ –4.2, now shifted downfield compared to free H₃B–NMe₃, $\Delta\delta$ +4.1.

DFT calculations³² have been employed to assess the different M–H₃B–NMe₃ interactions in **1**⁺ and **2**⁺, the cations of **1** and **2** respectively. Optimised geometries (Scheme 4) reproduce the more symmetric structure of **2**⁺ compared to the Ag–H₃B–NMe₃ moiety in **1**⁺. The calculations also highlight subtle changes in the B–H bond distances, in particular a lengthening of the B1–H1A and B1–H1B bonds in **2**⁺ (both 1.276 Å) relative to the shorter distance computed for the non-interacting B1–H1C bond (1.203 Å). In **1**⁺ the B–H distances

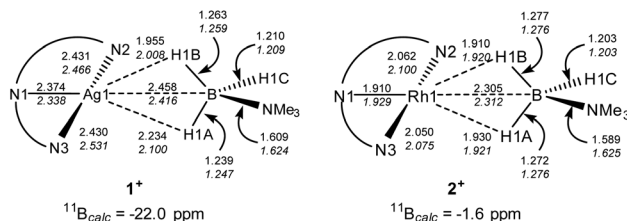


Scheme 2 Formation of the MeCN adducts by H₃B–NMe₃ displacement. [BAr^F₄][–] anions not shown.



Scheme 3 $^1\text{H}\{^{11}\text{B}\}$ NMR spectra of the H₃B–NMe₃ region of complexes **1** and **2** at 298 K and 183 K (CD₂Cl₂). * Mark signals due to NMe₃ groups.



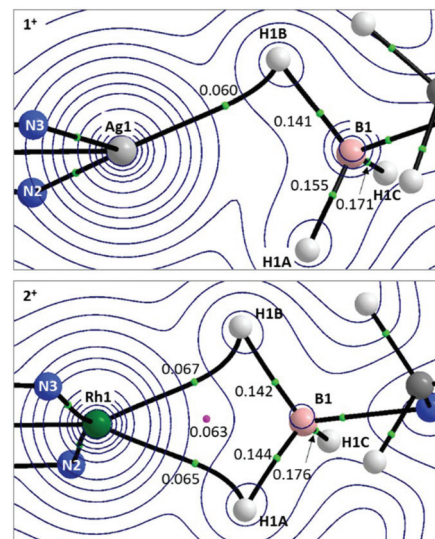


Scheme 4 Selected computed distances (Å) and ^{11}B chemical shifts for the cations of **1** and **2**. Distances in italics are from full optimisations; those in plain text from partial optimisations with heavy atom positions fixed from the experimental data.

follow the trend B1-H1B (1.263 Å) > B1-H1A (1.239 Å) > B1-H1C (1.210 Å) suggesting that B1-H1B and B1-H1A both interact with the Ag centre, albeit to a different extent. ^{11}B chemical shifts of δ -22.0 and δ -1.6 were computed for **1⁺** and **2⁺** respectively, and compare with δ -11.7 calculated for free $\text{H}_3\text{B-NMe}_3$ [$\Delta\delta$ -10.3 and +10.1 respectively]. Thus the experimental trend is reproduced, although the shifts relative to $\text{H}_3\text{B-NMe}_3$ are over-estimated in the calculations.

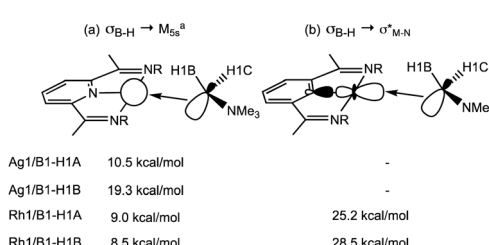
The fully optimised structures provided generally good agreement with the experimentally-determined metrics, but do over-estimate the $\text{M}\cdots\text{B1}$ and M-N distances. One of us³³ and others³⁴ have shown that geometries computed for isolated molecular species can deviate significantly from experimental structures derived from X-ray crystallography, especially where weak intramolecular interactions are at play in defining the observed geometry. Therefore, electronic structure analyses were based on geometries in which the heavy atoms were fixed in the positions determined experimentally with only the H atom positions being optimised. These structures (data in plain text, Scheme 4) show the same geometric trends for the B-H and M-H distances as the fully optimised structures, although the $\text{Ag}\cdots\text{H}_3\text{B-NMe}_3$ unit is somewhat more symmetrical than before. These structures were then analysed with Quantum Theory of Atoms in Molecules (QTAIM),³⁵ Natural Bond Orbital (NBO)³⁶ and Non-Covalent Interaction Plots (NCIPlots).³⁷

Details of the QTAIM molecular graphs for **1⁺** and **2⁺** are shown in Scheme 5. The asymmetry of **1⁺** is highlighted by the appearance of the single Ag1-H1B bond path. Accordingly, the B1-H1B Bond Critical Point (BCP) shows a reduced electron density, $\rho(r)$, indicative of donation to the Ag centre. However, $\rho(r)$ for the B1-H1A BCP is also lower than that for B1-H1C and this, along with the rather flat electron density topology between Ag1 and H1A , suggests a weak interaction may be present. For **2⁺** the symmetrical $\text{Rh}\cdots\text{H}_3\text{B-NMe}_3$ interaction is reflected in two similar bond paths, Rh1-H1B and Rh1-H1A , which encircle a Ring Critical Point (RCP). $\rho(r)$ values for the associated BCPs are similar to the Ag1-H1B BCP in **1⁺**, although the higher values of $\rho(r)$ associated with the Rh system suggest a stronger $\text{M}\cdots\text{H}_3\text{B-NMe}_3$ interaction in that case.



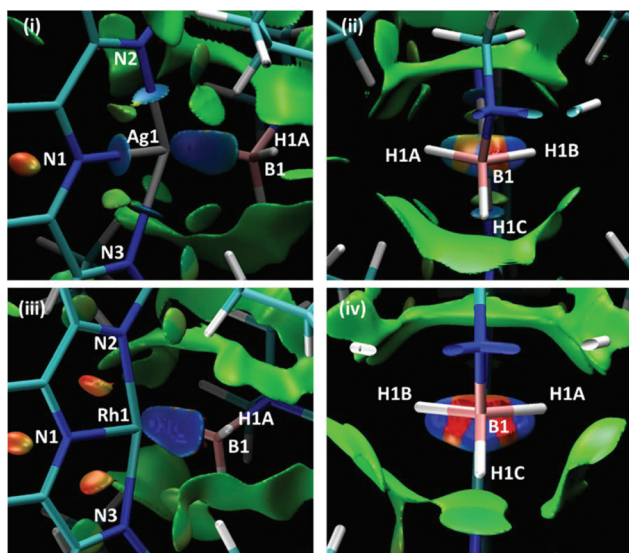
Scheme 5 Details from the QTAIM molecular graphs for **1⁺** (top) and **2⁺** (bottom), focussing on the $\text{M}\cdots\text{H}_3\text{B-NMe}_3$ regions. Contours are plotted in the M-H1B-H1A plane with selected atoms, bond paths and critical points lying above or below this plane being cloaked for clarity. Values of $\rho(r)$, the electron densities at selected BCPs (green circles) and RCPs (pink circles) are shown e \AA^{-3} . Full molecular graphs and Laplacian contour plots are available in the ESI.[†]

NBO calculations on **1⁺** highlight the Ag 5s orbital as the key acceptor in the $\text{Ag}\cdots\text{H}_3\text{B-NMe}_3$ interaction, with donation from both σ -orbitals associated with B1-H1A and B1-H1B (Scheme 6). Quantifying these through the 2nd order perturbation analysis confirms the latter donates more strongly ($\Delta E^{(2)} = 19.3 \text{ kcal mol}^{-1}$) but that donation from B1-H1A is also significant ($\Delta E^{(2)} = 10.5 \text{ kcal mol}^{-1}$). For **2⁺** the d⁸ electron count means a second low-lying acceptor becomes available in the form of the Rh1-N1 σ^* orbital, whereas the equivalent orbital for the d¹⁰ Ag^+ complex is filled. Donation into the Rh1-N1 σ^* orbital now dominates in **2⁺** and occurs to a similar extent (*ca.* 27 kcal mol⁻¹) from both B1-H1A and B1-H1B . These interactions are reinforced by weaker donation into the predominantly Rh 5s acceptor orbital (*ca.* 9 kcal mol⁻¹). The total donation is therefore approximately twice that computed for the $\text{Ag} \leftarrow \text{H1B-B1}$ interaction. In neither cation is there evidence for any significant $\text{M} \rightarrow \text{H}_3\text{B-NMe}_3$ back donation, as noted previously.²



Scheme 6 Key donor-acceptor interactions (illustrated for the B1-H1A bond) and 2nd order interaction energies (kcal mol⁻¹) derived from NBO analyses of **1⁺** and **2⁺**. ^a For **1⁺** the acceptor orbital is 97.7% 5s character; for **2⁺** it is 81.6% 5s and 18.4% 5d.





Scheme 7 NCIPlots for 1^+ and 2^+ viewed from (i)/(iii) above the pyridine ring and (ii)/(iv) down the $B1 \cdots M1$ axis; isosurfaces are generated for $s = 0.3$ au and $-0.07 < \rho < 0.07$ au.

Scheme 7 shows two views of the NCIPlots for both 1^+ and 2^+ . These plots highlight regions of weak interactions and are colour-coded from blue (most stabilising) through green (weakly stabilising) to red (most destabilising). Considering the Rh cation first, the broad blue region between Rh1 and the $H_3B \cdot NMe_3$ ligand indicates an area of significant stabilisation that runs approximately parallel to the H1A–B1–H1B bonds. When viewed down the $B1 \cdots Rh1$ axis (Scheme 7(iv)) a strong blue-red alternation is seen. Red regions flag up areas of destabilising charge depletion that are often associated with ring critical points (for example the red disks within the three rings of the L1Rh moiety). In this case the QTAIM study revealed a single RCP between Rh1 and B1 (Scheme 5), however, we have previously argued that the alternating blue-red-blue pattern indicates a stabilising interaction between a metal centre (here Rh1) and both centres of a σ -bond (here B1–H1A and B1–H1B).³⁸ This pattern is therefore consistent with the $H_3B \cdot NMe_3$ adopting an $\eta^2:\eta^2$ binding mode in 2^+ .

For 1^+ the NCIPlot displays a similarly shaped region between the Ag centre and the $H_3B \cdot NMe_3$ ligand and the blue-red-blue alternation in Scheme 7(ii) suggests a similar $Ag \leftarrow H1B \cdots B1$ interaction to those seen above with Rh. More asymmetry is again seen for the $Ag \cdots H_3B \cdot NMe_3$ interaction, especially in the lighter turquoise region between Ag1 and H1A and the less intense red associated with the B1–H1A bond when viewed down the $Ag \cdots B1$ axis (Scheme 7(ii)). Thus, the $Ag \cdots H_3B \cdot NMe_3$ interaction is intermediate between the $\eta^2:\eta^2$ geometry seen for 2^+ and the η^1 geometry proposed for species of type A and B in Fig. 1. This study also highlights the nuanced interpretation of the electron density topology that is available through the NCIPlot approach.^{39,40} The NCIPlot outcomes are also entirely consistent with the continuum of bond interactions that emerge from the NBO analyses.

Conclusions

By selecting a ligand framework, L1, that supports latent low coordinate complexes of Rh and Ag, the structures of, and bonding in, d^8 and d^{10} σ -amine borane complexes can be directly compared empirically and using computational methods. The d^8 -Rh(i) metal centre, which has access to an additional d-based unoccupied orbital compared with Ag(i), binds $H_3B \cdot NMe_3$ more strongly, as evidenced by: (i) a more definitive $\eta^2:\eta^2$ $M \cdots H_2B$ coordination motif, (ii) a significantly shorter $M \cdots B$ distance, (iii) a non-dissociative process for $H_3B \cdot NMe_3$ fluxionality, (iv) stronger $M \cdots H_3B$ interactions as measured by QTAIM and NBO analysis and (v) NCIPlots that highlight the more symmetric and stronger σ -bonding in the Rh-analogue. The coherence of all of these experimental and computational observations underscores the importance of deploying multiple analytical methodologies when studying this important class of complex.

Conflicts of interest

There are no conflicts to declare.

Acknowledgements

EPSRC EP/M024210/1 and SCG Chemicals Co. Ltd. Dr Nicholas Rees for DOSY experiments.

Notes and references

- 1 R. N. Perutz and S. Sabo-Etienne, *Angew. Chem., Int. Ed.*, 2007, **46**, 2578–2592.
- 2 M. Shimoi, S.-i. Nagai, M. Ichikawa, Y. Kawano, K. Katoh, M. Uruichi and H. Ogino, *J. Am. Chem. Soc.*, 1999, **121**, 11704–11712.
- 3 E. M. Leitao, T. Jurca and I. Manners, *Nat. Chem.*, 2013, **5**, 817.
- 4 A. L. Colebatch and A. S. Weller, *Chem. – Eur. J.*, 2019, **25**, 1379–1390.
- 5 D. Han, F. Anke, M. Trose and T. Beweries, *Coord. Chem. Rev.*, 2019, **380**, 260–286.
- 6 H. C. Johnson, C. L. McMullin, S. D. Pike, S. A. Macgregor and A. S. Weller, *Angew. Chem., Int. Ed.*, 2013, **52**, 9776–9780.
- 7 H. C. Johnson, R. Torry-Harris, L. Ortega, R. Theron, J. S. McIndoe and A. S. Weller, *Catal. Sci. Technol.*, 2014, **4**, 3486–3494.
- 8 T. Kakizawa, Y. Kawano and M. Shimoi, *Organometallics*, 2001, **20**, 3211–3213.
- 9 Y. Kawano, M. Hashiba and M. Shimoi, *Organometallics*, 2006, **25**, 4420–4426.
- 10 R. Dallanegra, A. P. M. Robertson, A. B. Chaplin, I. Manners and A. S. Weller, *Chem. Commun.*, 2011, **47**, 3763–3765.



11 A. E. Nako, A. J. P. White and M. R. Crimmin, *Dalton Trans.*, 2015, **44**, 12530–12534.

12 A. Hicken, A. J. P. White and M. R. Crimmin, *Inorg. Chem.*, 2017, **56**, 8669–8682.

13 E. A. Romero, P. M. Olsen, R. Jazzar, M. Soleilhavoup, M. Gembicky and G. Bertrand, *Angew. Chem., Int. Ed.*, 2017, **56**, 4024–4027.

14 F. Rekhroukh, L. Estévez, C. Bijani, K. Miqueu, A. Amgoune and D. Bourissou, *Angew. Chem., Int. Ed.*, 2016, **55**, 3414–3418.

15 M. Joost, S. Mallet-Ladeira, K. Miqueu, A. Amgoune and D. Bourissou, *Organometallics*, 2013, **32**, 898–902.

16 A. Ilie, C. I. Rat, S. Scheutzow, C. Kiske, K. Lux, T. M. Klapötke, C. Silvestru and K. Karaghiosoff, *Inorg. Chem.*, 2011, **50**, 2675–2684.

17 A. J. Clarke, M. J. Ingleson, G. Kociok-Köhn, M. F. Mahon, N. J. Patmore, J. P. Rourke, G. D. Ruggiero and A. S. Weller, *J. Am. Chem. Soc.*, 2004, **126**, 1503–1517.

18 V. C. Gibson, C. Redshaw and G. A. Solan, *Chem. Rev.*, 2007, **107**, 1745–1776.

19 S. D. Ittel, L. K. Johnson and M. Brookhart, *Chem. Rev.*, 2000, **100**, 1169–1204.

20 T. Jurca, S. I. Gorelsky, I. Korobkov and D. S. Richeson, *Dalton Trans.*, 2011, **40**, 4394–4396.

21 T. Jurca, S. Ouanounou, S. I. Gorelsky, I. Korobkov and D. S. Richeson, *Dalton Trans.*, 2012, **41**, 4765–4771.

22 M. L. Buil, M. A. Esteruelas, S. Niembro, M. Oliván, L. Orzechowski, C. Pelayo and A. Vallribera, *Organometallics*, 2010, **29**, 4375–4383.

23 M. M. D. Roy, M. J. Ferguson, R. McDonald and E. Rivard, *Chem. Commun.*, 2018, **54**, 483–486.

24 A. J. Martínez-Martínez and A. S. Weller, *Dalton Trans.*, 2019, **48**, 3551–3554.

25 E. L. Dias, M. Brookhart and P. S. White, *Organometallics*, 2000, **19**, 4995–5004.

26 E. L. Dias, M. Brookhart and P. S. White, *Chem. Commun.*, 2001, 423–424.

27 G. M. Adams, F. M. Chadwick, S. D. Pike and A. S. Weller, *Dalton Trans.*, 2015, **44**, 6340–6342.

28 N. J. Patmore, C. Hague, J. H. Cotgreave, M. F. Mahon, C. G. Frost and A. S. Weller, *Chem. – Eur. J.*, 2002, **8**, 2088–2098.

29 Addition of only 1 equivalent of MeCN to **1** causes broadening, but no significant chemical shift change, of the H_3B-NMe_3 signal that suggests a rapid ligand exchange is occurring, that favours the amine–borane adduct.

30 W. H. Bernskoetter, C. K. Schauer, K. I. Goldberg and M. Brookhart, *Science*, 2009, **326**, 553.

31 A. G. Algarra, L. J. Sewell, H. C. Johnson, S. A. Macgregor and A. S. Weller, *Dalton Trans.*, 2014, **43**, 11118–11128.

32 DFT calculations were performed with Gaussian 09 with optimisations using the BP86 functional with SDD basis sets and pseudopotentials on Rh and Ag and 6-31G** basis sets on all other atoms. ^{11}B chemical shifts were computed with the B3LYP functional with 6-311++g** basis sets on C, N, B and H atoms and included a correction of dichloromethane solvation (PCM approach). See ESI† for full details and references.

33 L. R. Collins, N. A. Rajabi, S. A. Macgregor, M. F. Mahon and M. K. Whittlesey, *Angew. Chem., Int. Ed.*, 2016, **55**, 15539–15543.

34 J. Moellmann and S. Grimme, *Organometallics*, 2013, **32**, 3784–3787.

35 R. F. W. Bader, *Atoms in Molecules: A Quantum Theory*, Clarendon Press, Oxford, 1994.

36 E. D. Glendening, J. K. Badenhoop, A. E. Reed, J. E. Carpenter, A. J. Bohmann, C. M. Morales, C. R. Landis and F. Weinhold, *NBO 6.0*, Theoretical Chemistry Institute, University of Wisconsin, Madison, WI, 2013.

37 J. Contreras-García, E. R. Johnson, S. Keinan, R. Chaudret, J.-P. Piquemal, D. N. Beratan and W. Yang, *J. Chem. Theory Comput.*, 2011, **7**, 625–632.

38 A. J. Martínez-Martínez, B. E. Tegner, A. I. McKay, A. J. Bukvic, N. H. Rees, G. J. Tizzard, S. J. Coles, M. R. Warren, S. A. Macgregor and A. S. Weller, *J. Am. Chem. Soc.*, 2018, **140**, 14958–14970.

39 C. Narth, Z. Maroun, R. A. Boto, R. Chaudret, M.-L. Bonnet, J.-P. Piquemal and J. Contreras-García, in *Applications of Topological Methods in Molecular Chemistry*, ed. R. Chauvin, C. Lepetit, B. Silvi and E. Alikhani, Springer International Publishing, Cham, 2016.

40 J. R. Lane, J. Contreras-García, J.-P. Piquemal, B. J. Miller and H. G. Kjaergaard, *J. Chem. Theory Comput.*, 2013, **9**, 3263–3266.

